An improved calibration methodology and uncertainty assessment in measurements of microbubble size and concentration

Stigter, R.; Fiscaletti, D.; Elsinga, G. E.; van Terwisga, T.; Westerweel, J.

DOI
10.1007/s00348-024-03929-3

Publication date
2025

Document Version
Final published version

Published in
Experiments in Fluids

Citation (APA)
Stigter, R., Fiscaletti, D., Elsinga, G. E., van Terwisga, T., & Westerweel, J. (2025). An improved calibration methodology and uncertainty assessment in measurements of microbubble size and concentration. *Experiments in Fluids*, *66*(1), Article 14. https://doi.org/10.1007/s00348-024-03929-3

Experiments in Fluids (2025) 66:14
https://doi.org/10.1007/s00348-024-03929-3

RESEARCH ARTICLE

An improved calibration methodology and uncertainty assessment in measurements of microbubble size and concentration

R. Stigter[1] · D. Fiscaletti[1] · G. E. Elsinga[1] · T. van Terwisga[1,2] · J. Westerweel[1]

Received: 6 August 2024 / Revised: 21 November 2024 / Accepted: 22 November 2024

Abstract
Interferometric particle imaging (IPI) is used to measure both the size distribution and concentration of microbubbles (with a diameter less than 100 micron) in water. Using a new method for calibration makes it possible to obtain quantitative results for the concentration of microbubbles. The results are validated using imaging with a long-range microscope shadowgraph (LMS). Estimates of the size distribution and concentration from both IPI and LMS agree within uncertainty limits. The relative uncertainty in the IPI concentration estimation is about 10% and is mostly due to the finite number of detected bubbles. It is shown that the performance of the bubble-image detection algorithm needs to be quantified to obtain a reliable estimate of the concentration obtained with IPI.

1 Introduction

Microbubbles of free and dissolved non-condensable gases are naturally present in water over a wide range of sizes and concentrations. The accurate measurement of the microbubble concentration spectrum represents an arduous technical challenge. However, knowledge of this spectrum is of great importance, for example in the development of models predicting cavitation inception and sound emission by cavitation (Friesch et al. 2002; Brandner et al. 2022).

There are several methods to characterize the microbubble content in a flow. We can roughly divide these into two classes, i.e., acoustical methods and optical methods. Examples of techniques belonging to the first family are cavitation susceptibility meter (CSM) (Oldenziel 1982) and the sonar (Medwin 1977; Thorpe 1982). Examples of techniques belonging to the second family are shadowgraphy, holography, and interferometry (Mees et al. 2010). In this study, an interferometric technique is applied to measure the concentration of microbubbles. Previous works using methodologies relying on interferometry to characterize microbubbles have adopted different nomenclatures, i.e., interferometric laser imaging technique (ILIT), Mie-scattering imaging (MSI), and interferometric particle imaging (IPI). Below, we refer to the applied technique as IPI.

We selected IPI for its proven effectiveness in studying cavitation inception (Brandner 2018). The technique is non-invasive, sensitive to microbubble sizes relevant to cavitation inception (10-100 μm), and accommodates low-concentration flows well due to its relatively large measurement volume with respect to shadowgraphic methods (Khoo et al. 2020). Unlike shadowgraphy and holography, IPI allows flexible positioning of the light source and working distance, enabling its use on model ships during towing tests (Birvalski and van Rijsbergen 2017, 2018). Recently, field measurement on a full scale vessel has been performed (Stigter et al. 2024).

Initially developed for measuring droplet and bubble sizes (König et al. 1986), IPI has been extensively studied for its precision in estimating microbubble diameters (Dehaeck and Van Beeck 2007). Reported uncertainties in bubble diameter typically lie within a few percent (Russell et al. 2020). However, despite this examination of diameter uncertainties, the uncertainty on the concentration measured by IPI remains unexplored. Besides a precise estimate of the microbubble diameter, an accurate definition of the measurement volume and a foolproof detection algorithm are necessary to determine the microbubble concentration. Especially the latter task is complicated by impurities in the flow.

✉ R. Stigter
m.stigter@tudelft.nl

[1] Department of Process & Energy, Faculty of Mechanical Engineering, TU Delft, Mekelweg 2, 2628CD Delft, The Netherlands

[2] MARIN, Haagsteeg 2, 6708PM Wageningen, The Netherlands

Published online: 31 December 2024

To the best of our knowledge, estimates of the microbubble concentration from IPI have never been successfully validated. Ebert et al. (2015) compare IPI with a phase-Doppler method, and the concentrations only agree to within an order of magnitude. Birvalski et al. (2019) determine the measurement volume of their setup independently, but the estimated concentrations differ strongly from a benchmark measurement technique. Another attempt to determine the measurement volume is made by Russell et al. (2020), but they do not validate their concentration measurement.

The aim of this work is to validate the concentration measurement from IPI and assess its uncertainty. For the validation, we compare with a benchmark technique, i.e., long-range microscopic shadowgraphy (LMS). We explain the working principles of both techniques and present a novel calibration methodology to obtain the measurement volume of IPI. Finally, from a thorough analysis, we identify the factors contributing the most to the uncertainties in the estimated concentration from IPI.

The paper is organized as follows: Section 2 explains the measurement setups used for this research. Section 3 describes the working principles and postprocessing algorithms for both LMS and IPI. The calibration and uncertainty assessment for both techniques are presented in Sect. 4. Section 5 presents and discusses the resulting size and concentration measurements. Section 6 summarizes the main conclusions of the study.

2 Experimental setup

A schematic overview of the experimental setup is shown in Fig. 1. The IPI equipment is oriented horizontally, consisting of a camera (LaVision Imager sCMOS CLHS), a laser (Azurlight Systems 488 nm CW Fiber), and an optical band-pass filter (FGB7, Thorlabs) that transmits blue light (435-500 nm). The LMS equipment is shown in vertical orientation, which includes a camera (LaVision Imager sCMOS CLHS), a back-light illumination (Schott KL1500 HAL), and an optical long-pass filter (FGL515M, Thorlabs) that transmits green, yellow and red light (cut-off wavelength of 515 nm).

The laser beam enters the glass water tank from below, pointing upwards. The long-pass filter in front of the LMS lens effectively blocks light scattered from the laser beam, ensuring no interference with the LMS image. Similarly, a band-pass filter placed in front of the interferometric particle imaging (IPI) lens prevents back-light illumination from being detected by the IPI setup. This strategic application of filters allows for simultaneous execution of both IPI and LMS measurements. Furthermore, careful alignment of the setups ensures that the measurement volumes of both techniques overlap, facilitating the identification of the identical microbubble in both IPI and LMS images.

This setup is used to perform two different types of measurements, i.e., a validation of the estimated size by IPI and a validation of the estimated concentration by IPI using LMS as a benchmark. In case of the size validation, a microfluidic chip with a T-junction is used to generate relatively large microbubbles (200-1000 µm diameter).

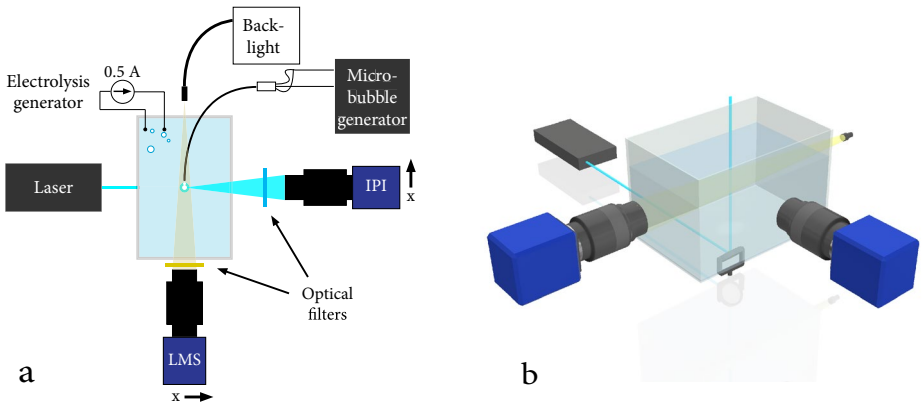

Fig. 1 (**a**) A schematic of the top-view of the experimental setup. The microbubble generator can generate relatively larger microbubbles (200–1000 µm) in a controlled manner. The electrolysis can generate relatively smaller microbubbles (20–150 µm) in an uncontrolled manner. Next to the cameras, the definitions of the x-axis for IPI and LMS are shown. (**b**) A schematic of the experimental setup viewed under an angle. The laser beam is reflected upwards into the water tank

The size and generation frequency is set by a pressure controller (Elveflow OB1). The chip is able to generate only a few microbubbles per second, which enables capturing a single microbubble per image. For this measurement, the IPI and LMS setup use the same lens (Nikon AF Micro Nikkor 105 mm 1:2.8).

In case of the concentration validation, electrolysis is used to generate a cloud of relatively small microbubbles (diameter < 200 µm). A mechanical stirrer is added to distribute the microbubbles throughout the glass tank and increase their residence time in the tank. The electrodes (Sigma-Aldrich) are two graphite rods with a thickness of 6 mm and a length of 150 mm. A power supply generates a constant current of 0.5 A. Because these microbubbles are relatively small, the magnification of the LMS setup is increased to 2.7 using a telescopic lens (Navitar), which consists of a zoom lens (1-60123) and an adapter (1-62922).

Sample images acquired for size validation and for concentration validation are shown in Fig. 2 and in Fig. 3, respectively. Figure 2a shows a typical fringe pattern from a microbubble. However, the fringe pattern from IPI can be distorted in a number of ways. First, due to interference of light scattered from nearby microbubbles, a tilted fringe pattern can emerge on top of the correct fringe pattern (Fig. 2b). Second, when a small object is located between the microbubble and the lens, an image is created that we refer to as a hologram, which is projected onto the microbubble image (Fig. 2c). Filtering the water from particles larger than 4 µm could reduce the distortion by holograms.

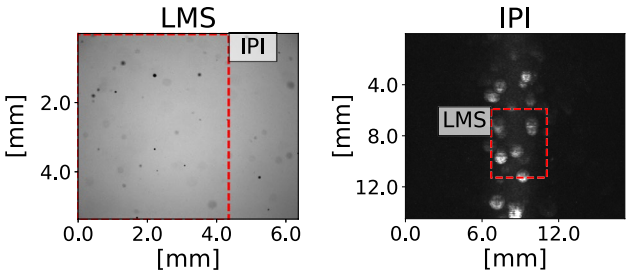

Fig. 3 Typical images of the microbubbles generated by electrolysis. The red box in the latter images highlights the measurement volume of the other technique. Therefore, microbubbles inside these boxes are visualized by both techniques

Particles influence the IPI image as well. Non-spherical objects are known to generate speckle patterns (Fig. 2d). These speckle patterns hamper the detection of fringe patterns from microbubbles. Spherical particles create a fringe pattern that is identical to that from a microbubble (Fig. 2e), resulting in false counts.

3 Method

3.1 Interferometric particle imaging (IPI)

Interferometric particle imaging is based on the Mie-scattering pattern generated when a monochromatic, coherent light source hits a spherical object, where the object has a diameter significantly larger than the wavelength of the light.

Fig. 2 Typical examples of fringe patterns in IPI images and corresponding LMS images

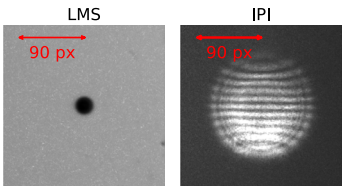

(a) A typical fringe pattern from a spherical bubble.

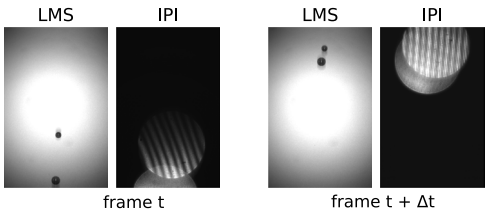

(b) A tilted fringe pattern changing orientation over time as a result of proximity between two microbubbles.

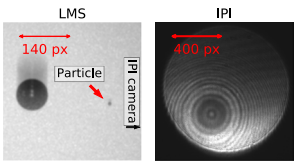

(c) A small particle in the proximity of a microbubble generating a hologram in the microbubble image from IPI.

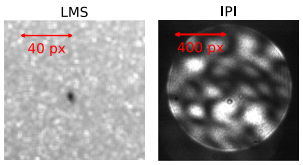

(d) A non-spherical particle producing a speckle pattern in the IPI image.

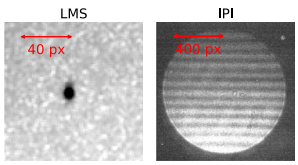

(e) A spherical hollow glass bead producing a fringe pattern similar to that typically obtained from a microbubble.

The diffraction pattern is visible as a fringe pattern in the out-of-focus image of the spherical object.

The complete Mie-scattering solution for a spherical object is mathematically complex. However, the correlation between the object diameter (d) and the number of fringes in the diffraction pattern (N_{fr}) can be described with a linear relationship. From an IPI image, N_{fr} can be found by dividing the image diameter (D) by the wavelength of the fringes in the image (λ), which leads to the following expression for the object diameter,

$$d = K\frac{N_{fr}}{\alpha} = K\frac{D}{\alpha\lambda}, \tag{1}$$

where K is a proportionality constant and α is the collection angle. This relation also applies to microbubbles, provided that they are spherical. In Fig. 4, the quantities λ and D are shown in a sample IPI image of a microbubble.

As pointed out by Graßmann and Peters (2004), both D and α vary as a function of the out-of-focus distance z_0. The exact relationship for α and D as function of z_0 depends on the optics used in the measurement. We can approximate these relationships for the optics used by means of a double-lens model. This model contains six degrees of freedom, i.e., the distance between focal plane and front lens (z_1), the distance between the lenses (Δz), the distance from rear lens to screen (z_2), the aperture diameter (D_a), and the focal length of both the front lens and the rear lens (f_1 and f_2, respectively).

Figure 5 shows the double-lens model for an IPI setup visualizing a microbubble in water. In this case, two degrees of freedom are added, i.e., the distance between the front lens to the glass having air as medium, and the thickness of the glass. These distances can be measured in our setup. The distance from focal plane to front lens is increased in our setup with respect to the case in air (z_1) due to the larger refractive index and is referred to as $z_{1,m}$, as can be seen in Fig. 5.

The model provides relationships for the collection angle α, the image size D, and the magnification M as a function of z_0. These relationships depend on z_1 instead of $z_{1,m}$. The correction for the influence of the different media is incorporated by multiplying z_1 by the refractive index n of the water, where the microbubble is located:

$$\alpha(z_0) = 2\tan^{-1}\left(\frac{D_a/2}{z_1 n + z_0}\right), \tag{2}$$

$$D(z_0) = \left|M_0 D_a \frac{z_0}{z_1 n + z_0}\right|, \tag{3}$$

$$M(z_0) = M_0 \frac{z_1 n}{z_1 n + z_0}, \tag{4}$$

where M_0 is the magnification at $z_0 = 0$.

The advantage of this approach is that a calibration of the expression for $M(z_0)$ is sufficient to determine $\alpha(z_0)$ and $D(z_0)$. A calibration of $M(z_0)$ provides the parameters z_1 and M_0, which are the only unknowns in Eqs. 2 and 3. The calibration of $M(z_0)$ can be done by moving a calibration plate in front of the lens, to certain positions of z_0. This procedure is relatively easy, as opposed to the more difficult procedure used to calibrate $\alpha(z_0)$ directly.

The position z_0 of a microbubble is not known a-priori, but D can be computed directly from the microbubble images. By inverting Eq. 3, z_0 can be calculated from D, after which z_0 can be inserted in Eq. 2 to find α for each

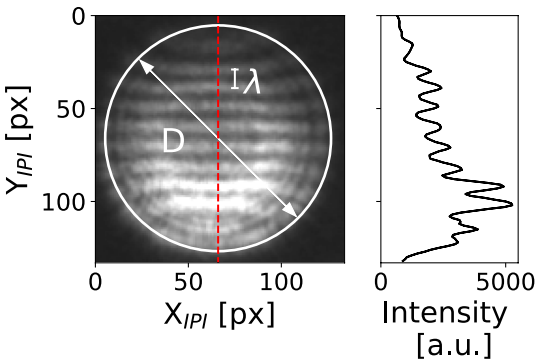

Fig. 4 Graphical definition of the parameters used to estimate the microbubble diameter from IPI, see text

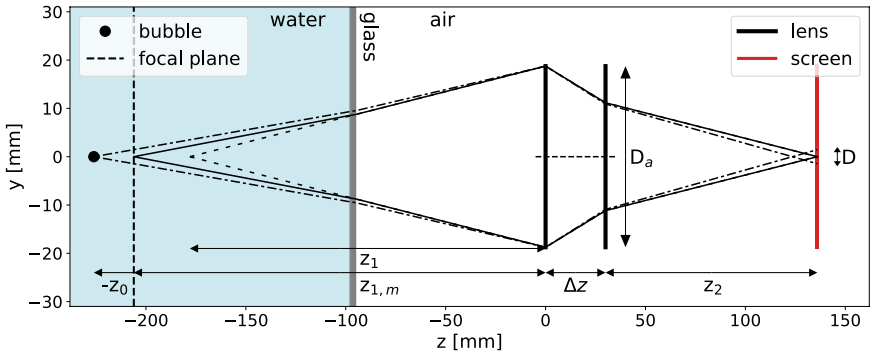

Fig. 5 A schematic overview of the double-lens model. This arrangement models our IPI setup, with the optics in air and the microbubble in water, separated by a transparent medium. The larger refractive index of the water causes an increase in working distance from z_1 to $z_{1,m}$. z_0 is positively defined in the direction of the lenses

individual microbubble. It is important to stress that a single-lens model would not be adequate to model the behavior of the optics we use, because it does not correctly capture the relationships for $M(z_0)$, $\alpha(z_0)$ and $D(z_0)$.

Russell et al. (2020) discuss several methods to determine the fringe wavelength λ, i.e., the peak-finding method, the fast Fourier transform (FFT), the auto-correlation, and the wavelet transform. They conclude that the auto-correlation method is the most accurate one, especially for the relatively small microbubbles, with the FFT method giving almost identical results. However, we selected a 2-D FFT method, because it provides the orientation of the fringe pattern as additional information. Using this orientation, it is possible to distinguish between microbubble images and images from other objects. These aspects are discussed in further detail later in the paper.

The measurement volume of IPI is defined by applying a minimum threshold (I_{th}) on the intensity (I) of the microbubble images. This intensity is proportional to the laser beam intensity profile, the microbubble diameter squared (d^2) (Zangwill 2013, chapter 21.5.2), and inversely proportional to the microbubble image diameter squared ($1/D^2$). The latter effect describes the fact that when the image size is enlarged over a larger image area by defocusing, the light has to be distributed over a larger area, resulting in a lower image intensity. Assuming the laser beam intensity profile as Gaussian, the microbubble image intensity is found to be:

$$I(\delta) = \tilde{I}_0 \exp\left\{-\left(\frac{\delta}{\delta_b}\right)^2\right\}\frac{d^2}{D^2}, \tag{5}$$

where $\tilde{I}_0$ is a proportionality constant, δ_b is a measure for the width of the laser beam, and δ the distance of the microbubble position to the laser beam axis in a polar coordinate system.

Microbubbles having an intensity larger than I_{th} are included in the estimation of the measurement volume, so the edge of the measurement volume is defined by microbubbles having an intensity exactly equal to I_{th}. Rewriting Eq. 5 gives the distance from the laser beam axis to the edge as

$$\delta_{edge} = \delta_b\sqrt{\ln\left(\frac{\tilde{I}_0}{I_{th}}\frac{d^2}{D^2}\right)}. \tag{6}$$

Clearly, the measurement volume depends on the diameter of the microbubble. The effect of this dependency is shown later (Fig. 12b).

The variation in D due to the microbubble position z_0 causes the volume to be elliptical rather than circular, slightly stretched toward the focal plane. The stretching of the measurement volume toward the focal plane happens because for decreasing z_0 the microbubble images become relatively much brighter due to their relatively smaller size D ($I \propto 1/D^2$), which leads to exceeding the threshold intensity I_{th} over a wider area when approaching the focal plane. On this regard, Fig. 6 shows the cross section of the measurement volume along a plane orthogonal to the camera lens. The circle formed by the dashed line represents the cross section of the measurement volume when D is assumed to be constant, while the ellipse formed by the solid line represents the measurement volume for varying D.

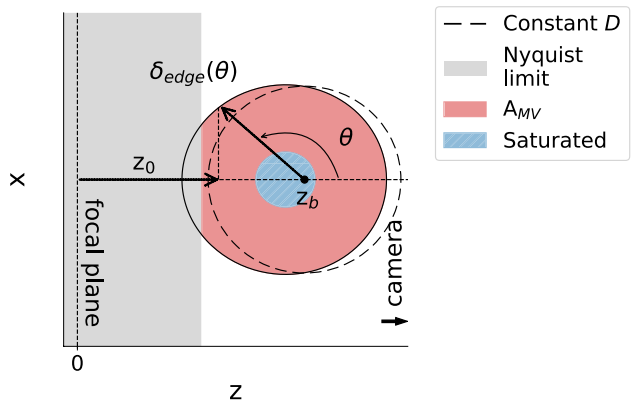

Fig. 6 The cross section of the measurement volume (A_{MV}) along a plane orthogonal to the lens. Because D varies with z_0, A_{MV} is elliptical. Both saturation of the sensor and the Nyquist limit reduce the area of A_{MV}. The graph shows the definition of a coordinate system, which can be used to calculate the area of the A_{MV}. z_b is the position of the laser beam center with respect to the focal plane. All areas highlighted in the graph depend on the microbubble diameter

Figure 6 shows how the area of the cross section of the measurement volume can be computed. From this figure, we see that $z_0 = z_b + \delta_{edge}(\theta)\cos(\theta)$, where z_b is the out-of-focus distance of the laser beam axis. Because D depends on z_0, it also depends on δ_{edge}. Substitution of $D(\delta_{edge}, \theta)$ in Eq. 6 results in an implicit relation for δ_{edge}. Solving this relation gives δ_{edge} as a function of θ. Finally, the area of the cross section, A_{MV}, can be computed by integration of $1/2\,\delta_{edge}(\theta)^2$ over θ. To obtain the total measurement volume, this area should be multiplied by the length (L) over which the laser beam appears in the image.

The smallest λ that can be measured is theoretically set by the Nyquist limit, which is equal to two pixels (Nobach et al. 2002). Closer toward the focal plane (smaller z_0), D decreases and the fringe pattern is compressed. When z_0 is small enough, the fringe spacing will be smaller than the Nyquist limit and the correct diameter can no longer be determined. This results in a reduction of A_{MV}, which is represented by the gray area in Fig. 6. If d is large enough, this gray area surpasses the red area, and A_{MV} becomes equal to zero.

A fringe spacing that is smaller than the Nyquist limit will lead to an underestimation of the corresponding

microbubble diameter due to aliasing. If a significant amount of microbubbles has a diameter that is larger than the maximum detectable diameter of the IPI setup, the aliasing will influence the estimated microbubble concentration. It is, however, important to note that, with reference to Fig. 6, only the microbubbles that are located in the portion of measurement volume where the gray region intersects with the ellipse described by $\delta_{edge}(\theta)$ are exposed to aliasing.

The maximum detectable microbubble diameter, d_{max}, is found when the area represented by the Nyquist limit (the gray area) exactly covers A_{MV} (the red area). The position of this microbubble will therefore be on the $\theta = 0$ axis, at the edge at the right-hand side of A_{MV} in Fig. 6. With $\theta = 0$, the coordinate systems of the lens and the laser beam can be related as $z_0 = z_b + \delta$. The intensity I of a microbubble has a fringe distance equal to the Nyquist limit ($\lambda = 2$) and is located at a position δ can be found using Eq. 5, where Eq. 1 can be used to eliminate d/D, and Eq. 2 to determine the collection angle:

$$I(\delta) = \frac{K^2 \tilde{I}_0}{16}\left[\tan^{-1}\left(\frac{D_a/2}{z_1 n + z_b + \delta}\right)\right]^{-2} e^{-\frac{\delta^2}{\delta_b^2}}, \tag{7}$$

where we assume $\theta = 0$. When setting this equation equal to I_{th}, two solutions can be found for δ, i.e., one close to the object focal plane and one closer to the lens with respect to the laser beam center. The latter one corresponds to the position of the microbubble with the maximum diameter. This position can be used to determine α and D of this microbubble from Eqs. (2 and 3), and the maximum microbubble diameter d_{max} using Eq. 1.

A_{MV} can also be reduced by image saturation: microbubbles can scatter so much light that the microbubble image is (partly) saturated. For a Gaussian beam intensity profile, this typically happens when the microbubble is close to the beam center. The corresponding area can be calculated by replacing I_{th} in Eq. 6 with I_{BD}, i.e., the bit-depth intensity of the camera; see the blue shaded area in Fig. 6. The diameter for which saturation occurs can be approximated using Eq. 5, assuming saturation to happen at the laser beam center ($\delta = 0$, $z_0 = z_b$), as follows

$$d_S = D(z_b)\sqrt{\frac{I_{BD}}{\tilde{I}_0}}. \tag{8}$$

To measure larger microbubbles at fixed D, one can reduce the laser power or use an imaging sensor with a higher full well capacity.

The IPI technique also presents a limit on the smallest diameters that can be measured. This limit typically depends on the lowest number of detectable fringes. This is approximately two, which corresponds to a fringe spacing of $\lambda_{max} = D/2$. From Eq. 1, we see that the corresponding lower microbubble diameter limit is then given by

$$d_{min} = 2\frac{K}{\alpha(z_b)}. \tag{9}$$

Furthermore, Eq. 6 shows that δ_{edge}, and correspondingly, the measurement volume becomes zero if the microbubble diameter is small enough. This introduces an additional lower limit on the microbubble diameter, which can be estimated by setting $\delta_{edge} = 0$ in Eq. 6 as

$$d_{min,I} = D(z_b)\sqrt{\frac{I_{th}}{\tilde{I}_0}}. \tag{10}$$

This expression shows that, in order to decrease the minimum detectable microbubble diameter, one could use either a stronger laser (increasing $\tilde{I}_0$), or move the laser beam closer to the focal plane (reducing $D(z_b)$), or reduce the threshold value I_{th}. However, when I_{th} is close to the background noise level of the image, detection algorithms typically become less accurate.

3.2 Analysis of IPI images

We use the Hough gradient method (Duda and Hart 1972) to identify microbubble images within each IPI image. Before applying this method, we subtract a background image and apply a Gaussian blur filter with a 5 px kernel size. After this, we apply a minimum intensity threshold and calculate the edges from the remaining objects. Finally, the Hough gradient method determines the position and area of the microbubble images based on the previously detected edges[1].

A first estimate of D can be gained from the area A of the microbubble image, using the relationship $D \approx 2\sqrt{A/\pi}$. However, this estimate depends on the intensity of the microbubbles with respect to the threshold value and on possible overlapping images. Therefore, we apply a more accurate method, the steps of which are graphically elucidated in Fig. 7. We identify a cross section in the middle of the microbubble image, in the direction parallel to the fringe pattern. The high-frequency components are previously removed using a Gaussian filter with a 5 px kernel size, resulting in a smooth envelope. The maximum gradient of the envelope corresponds to the left edge, while the minimum gradient corresponds to the right edge; see Fig. 7c. The estimate of the edge positions is improved using a Gaussian fitting procedure on the 3 pixels around the extremes in the gradient (Shinpaugh et al. 1992). From these edges,

[1] We use the Hough gradient method as implemented in the Python distribution of *OpenCV* (Bradski 2000)

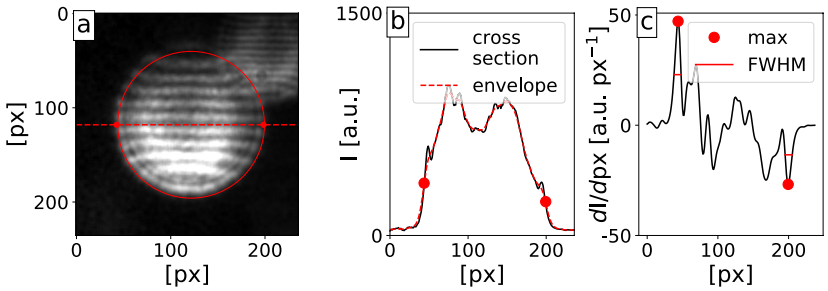

Fig. 7 Estimation method for D. (**a**) A cross section of the middle of the microbubble is selected, perpendicular to the fringe pattern; (**b**) a smooth envelope is calculated from the original signal; (**c**) the derivative of the envelope is determined. The maximum of the derivative corresponds to the left edge, and the minimum to the right edge

we compute D as the distance between the edges, and as an uncertainty for this estimate we take the full width at half maximum (FWHM).

An estimate of the scattering intensity is obtained from taking the 95-percentile of the intensity of the pixels within the microbubble disk, following Russell et al. (2020).

The fringe spacing is determined using the 2-D FFT method, which provides the orientation of the fringe pattern as an additional parameter. Before we can apply the FFT method, the microbubble image should be pre-processed. These steps are graphically elucidated in Fig. 8. First, we remove parts of overlapping microbubbles (Fig. 8b). Second, to reduce the effect of curved fringes at the microbubble image edge, we inscribe the largest possible rectangle that fits the microbubble image after the removal operation. This results in a rectangular image containing only the fringe pattern (Fig. 8c). Third, we compute an envelope of the microbubble image using an uniform filter with a kernel size of 30% of the microbubble image size. The envelope is subtracted from the square image to reduce any large-scale intensity gradients. The 30% is found to be a convenient value to remove the large-scale intensity gradients, while keeping the fringe pattern intact. Fourth, the mean intensity is subtracted to remove the DC peak in the FFT pattern. Finally, the resulting image is multiplied by a 2D Hann filter to reduce spectral leakage (Fig. 8d).

The third step necessitates some further explanations. This step is effectively a high-pass filter, and it is important because there are large intensity differences between the side of the microbubble where the laser beam enters and the side where the beam leaves the microbubble. This is especially the case when the scattering angle is 90° and the laser beam is parallel polarized. The application of this high-pass filter might lead to a complete removal of the signal when the fringe pattern has a relatively large spacing. However, without this operation large-scale intensity gradients typically have more spectral weight than the fringe pattern itself, which makes it impossible to resolve the actual fringe spacing.

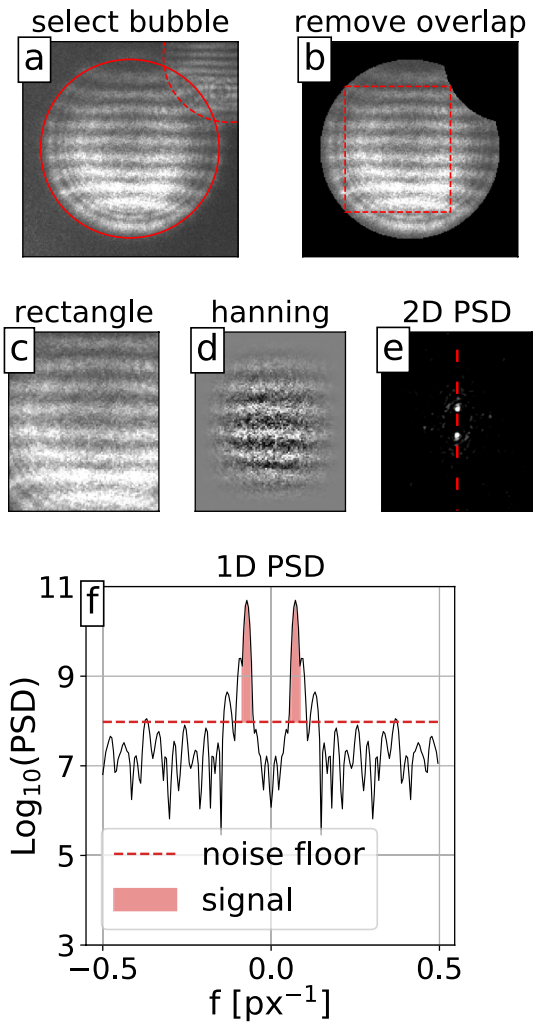

Fig. 8 Steps of the pre-processing and 2D-FFT method to estimate the fringe wavelength and the singal-to-noise ratio

After these operations, the 2-D FFT algorithm is applied, and the power spectral density (PSD) is computed (Fig. 8e). The position of the PSD maxima is approximated using a 1-D Gaussian interpolation method in both x and y-direction

(Adrian et al. 1991). From the comparison between the peak positions and the DC position, we obtain the fringe spacing frequency and the orientation of the fringe pattern. To determine the signal-to-noise ratio (SNR), we select the points that are on a line through the two peaks (Fig. 8f). From these points, the signal power and noise power are determined, and the SNR is computed according to

$$\mathrm{SNR} = 10 \log_{10} \left(\frac{\text{signal power}}{\text{noise power}} \right), \tag{11}$$

where the signal power is the sum of the harmonic contributions of the signal multiplied by the frequency resolution Δf of the PSD, and the noise power is defined as all other harmonic contributions multiplied by Δf.

The length of the rectangle cutout (Fig. 8c), N_s, is an important parameter. At first, this parameter is necessary to determine the uncertainty in λ as it describes the number of samples of the PSD. Moreover, it also increases the minimum detectable microbubble diameter, d_{min}. Typically, $N_s \leq D$, resulting in less space to fit the minimum number of two fringes.

3.3 Long-range microscopic shadowgraphy (LMS)

We use LMS to validate the estimates of microbubble concentration from IPI. With this technique, it is possible to obtain the 3-D microbubble position using a single camera. After calibration of the magnification factor, it is possible to obtain the 2-D location of the microbubble in the object plane. Additionally, the sharpness of the microbubble image contains information about the position of the microbubble perpendicular to the object plane (the out-of-focus distance z_0) (Pentland 1987), resulting in the full 3-D microbubble position. When the full 3-D position of the microbubble is known, it is possible to determine the microbubble concentration and compare this with the IPI concentration estimation.

The intensity field of the image of a point object can be described using a *point-spread function* (PSF). For non-monochromatic (white) and incoherent light, the PSF can be approximated by a 2-D Gaussian function (Lebrun et al. 1993). The sharpness of the image is related to the width, χ, of the Gaussian PSF, relating χ to the out-of-focus distance z_0. Fdida and Blaisot (2010) show that χ is proportional to z_0 for relatively small values of χ (and thus z_0).

Fdida and Blaisot (2010) define χ as proportional to the edge width ΔR,

$$\chi = \frac{\Delta R}{p_r(C_M^0)}, \tag{12}$$

where p_r is a third-order polynomial function of C_M^0, which is the normalized Michelson contrast. $p_r(C_M^0)$ corrects for both the transparency of the microbubble object and relative size of the microbubble image.

The Michelson contrast C_M is typically used in images where both bright and dark features are equivalent and take up similar fractions of the area. It is defined as

$$C_M = \frac{1 - I_{min}/I_{max}}{1 + I_{min}/I_{max}}, \tag{13}$$

where I_{min} and I_{max} represent the highest and lowest intensities in the image, respectively. The maximum contrast C_M is set by the transparency τ of the microbubble image, which is defined as the minimum value of I_{min}/I_{max} of all microbubbles detected. The normalized contrast, C_M^0, is helpful, because it removes the influence of the transparency on the contrast. C_M^0 is defined as

$$C_M^0 = \frac{C_M}{(1 + C_M)(1 - \tau) - C_M}, \tag{14}$$

and its value ranges between one (maximum darkness, τ) and zero (no detectable contrast).

C_M^0 decreases when the (blurred) edge of the microbubble image extends into the image. This happens when z_0 is large, or when the microbubble image is small. The contrast is thus influenced by χ and by the radius R of the microbubble image. C_M^0 affects the calculation of χ as well as the microbubble image radius R. Fdida and Blaisot (2010) introduce a function $p_l(C_M^0)$ to correct for the influence of C_M^0 on the estimated radius R, resulting in the following relation for the microbubble diameter in object plane

$$d = 2\, R\, p_l(C_M^0). \tag{15}$$

Fdida and Blaisot (2010) define R as the radius at a certain intensity level I_l of the microbubble image, defined as an intensity level between the minimum intensity I_{min} and the background intensity I_{max}, i.e.

$$I_l = I_{min} + l\big(I_{max} - I_{min}\big), \tag{16}$$

with l denoting the intensity level. The microbubble radius R_l corresponding to the level l is defined as $R_l = R(I_l)$. We compute R_l by counting all pixels with an intensity below I_l. This results in an area from which we obtain the radius as follows

$$R_l = \sqrt{A/\pi}. \tag{17}$$

Fdida and Blaisot (2010) give $l = 0.61$ as the optimal intensity level to evaluate the microbubble radius and use $R_{0.77} - R_{0.25}$ as the definition of the edge width ΔR. Figure 9

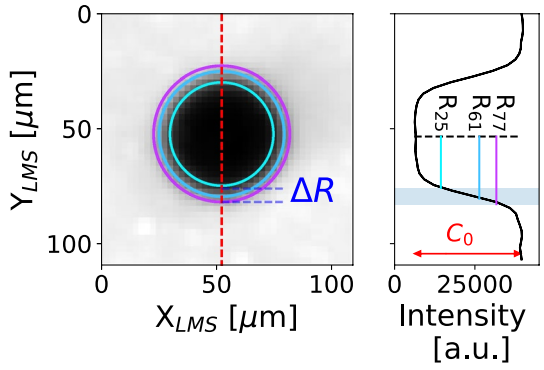

Fig. 9 Graphical definition of the parameters used to estimate the microbubble diameter from LMS

shows these intensity levels in a typical LMS microbubble image.

Because χ is proportional to z_0, a maximum limit (χ_{max}) on χ defines the depth of the measurement volume, Δz_0. The criterion for the depth of the measurement volume is thus given by

$$\chi \leq \chi_{max}. \tag{18}$$

The total measurement volume is calculated by multiplying Δz_0 by the area of the field of view in the object domain.

Fdida and Blaisot (2010) argue that this criterion in Eq. 18 is independent of the diameter of the object. However, this assumption only holds for relatively small values of χ. When χ becomes larger than the microbubble image radius R, the microbubble image contrast reduces. If the contrast is too small, microbubble detection is avoided. Because this effect depends on R, it leads to a bias toward larger microbubbles in the concentration. Therefore, we define χ_{max} as the largest value of χ for which this bias effect does not occur at the smallest microbubble diameters we intend to measure.

3.4 Analysis of LMS images

To prepare the images for analysis, we subtract a background image and apply a Gaussian blur filter with a 5 px kernel size. The next step is to determine the locations and to estimate the areas of the microbubble images. We use a threshold-based algorithm, where all objects below a certain intensity are labeled[2] and their center positions are determined. The radius R is approximated from the labeled area of the microbubble image, using Eq. 17.

Individual microbubbles are selected by cropping regions of size $1.5R$ around their centers. The cropped region is always larger than the microbubble image, which makes it possible that microbubbles located in the close proximity are also partly included. This can deteriorate the estimate of R, because such estimate is based on the number of pixels having an intensity below a certain intensity I_l. To overcome this limitation, we apply the labeling algorithm again on this cropped region and select the object that is the closest to the center of the region.

After the selection and filling of the microbubble images, we determine I_{min} and I_{max}, and subsequently $I_{0.25}$, $I_{0.61}$, and $I_{0.77}$, using Eq. 16. From the obtained intensity levels, we compute the corresponding radii R_l.

The images of the microbubbles generated by the microfluidic chip are found to be characterized by a bright spot in the center. This anomaly can be associated with the backlight illumination from the LED panel. Because the estimate for R_l is defined by the number of pixels below I_l, this bright spot causes an underestimation of R_l. We solve this by filling the selected region in the image using a binary filling method[3]. For a good performance of the filling method, the lower level is increased from 0.25 to 0.45, which also implies a different $p_r(C_M^0)$ polynomial.

To distinguish between images of particles and of microbubbles, we introduce a parameter that quantifies the deviation from circularity of the microbubble or particle image, as suggested by Blaisot and Yon (2005):

$$\epsilon = \frac{L_{min}}{L_{max}}. \tag{19}$$

To estimate the value of ϵ for each image, we select all pixels having an intensity level below 0.50 (i.e., $I_{0.50}$). Then, we crop this region along the edges. L_{min} is the shortest chord of this cropped region passing through its center, whereas L_{max} is the longest one. We assume that microbubbles are spherical, and they should therefore have a value of ϵ close to 1. By selecting only objects with $\epsilon \geq 0.9$, we can discard most of the odd-shaped objects.

4 Calibration and uncertainty assessment

4.1 Calibration of IPI

In this section, we explain the calibration procedure of K, α, $\tilde{I}_0$ and δ_b. Moreover, we assess the uncertainties in the estimation of these parameters and additionally in D, SNR, and λ. Finally, we quantify the uncertainty due to erroneous detection in the post-processing algorithm.

[2] We use the *connectedComponentsWithStats* algorithm from *OpenCV* (Bradski 2000) for this task.

[3] We use the *ndimage* package implemented within the *SciPy* library (Virtanen et al. 2020)

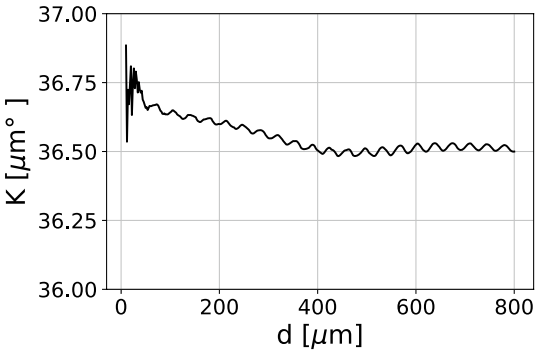

Fig. 10 The relationship between the proportionality constant K and the microbubble diameter. This relationship is determined using a numerical simulation of the fringe pattern from microbubble images. In this simulation, the Mie-scattering pattern for a certain scattering angle and the collection angle is calculated to determine the fringe pattern

We calibrate K by simulating the fringe pattern of microbubble images over a large range of microbubble diameters and evaluating the corresponding fringe spacing using the 2D-FFT method[4]. The resulting relation between K and D is shown in Fig. 10. This figure shows that K varies only little with d. The average value of K over a diameter range of 10-800 μm is 36.60 ± 0.07 μm°.

We calibrate the magnification of the lens by moving a calibration plate over a distance of -5 mm $\leq z_0 \leq 5$ mm. This results in $M_0 = 0.977 \pm 0.021$. Using Eq. 4 and the calibration relation for $M_0(z_0)$, we find $z_1 = 177.7 \pm 3.1$ mm. This corresponds to a collection angle of $9.05 \pm 0.160°$ for an object at the focal plane.

For validation of this result, we calibrate the collection angle α in a similar way as done by Russell et al. (2020). A thin plate with a hole is placed between the laser beam and the lens, so that it acts as the optical aperture of the system. When a microbubble moves through the laser beam, the size of its image D is defined by the diameter d_{hole} of the hole in the plate. Because the position of the laser beam and plate are known, the collection angle for this situation can be determined. By comparing the microbubble image diameter of the case including the plate with the case without plate, the collection angle of the optical system can be determined. From this calibration procedure, we find $\alpha = 10.38 \pm 0.27°$, for $z_0 = -32.46$ mm. From Eq. 2 and the value of z_1 found, our model predicts a collection angle of $\alpha = 10.48°$ for this value of z_0, which is within the uncertainty range of the calibration.

[4] We compute the fringe pattern using the Python library *PyMieScatt* (Sumlin et al. 2018)

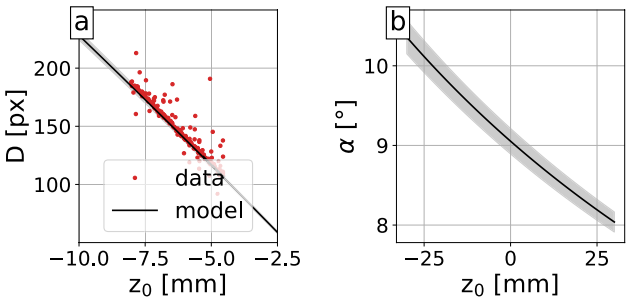

Fig. 11 The microbubble image diameter (**a**) and collection angle α (**b**) as a function of the out-of-focus distance. The shaded areas correspond to a deviation of one standard deviation

We validate the parameters in Eq. 3 by obtaining z_0 from the LMS camera for 281 IPI microbubbles. The result is shown in Fig. 11a. The line in the graph represents Eq. 3, with values for M_0 and z_1 as found above. Similarly, we can compute α as a function of z_0 using Eq. 2, with the result shown in Fig. 11b.

An estimate in the uncertainty in D is given by the widths of the peaks in the gradient plot (Fig. 7). When we assume that these peaks are Gaussian, the standard deviation is related to the FWHM as $\mathrm{FWHM} = 2\sqrt{2\ln 2}\sigma$. Combining the widths of both peaks results in

$$\sigma_D = \frac{1}{2\sqrt{2\ln 2}}\sqrt{\mathrm{FWHM}_{\mathrm{left}}^2 + \mathrm{FWHM}_{\mathrm{right}}^2}. \tag{20}$$

The uncertainty in λ is based on the Cramer–Rao bound, which states that the minimum variance in the estimated fringe spacing is given by (Ibrahim et al. 1991)

$$\sigma_f^2 = \frac{12}{(2\pi)^2 \mathrm{SNR} N_s (N_s^2 - 1)} f_s^2, \tag{21}$$

where SNR is the signal-to-noise ratio defined in Eq. 11, N_s the number of samples (i.e., pixels), and f_s the sampling frequency of the FFT signal. In our case, the sampling frequency is equal to 1/px. The fringe spacing λ is found by dividing N_s over the fringe spatial frequency f. Assuming no uncertainty on N_s, the uncertainty in the fringe spatial frequency, σ_f, is equal to σ_λ. It has been shown that Eq. 21 is only valid when the product $\mathrm{SNR}N_s$ is larger than 15 dB (Shinpaugh et al. 1992).

The parameters corresponding to the laser illumination, $\tilde{I}_0$ and δ_b, are calibrated using a fitting procedure. Figure 12a shows the parameter ID^2/d^2 versus the x position of the microbubbles in the laser beam. According to

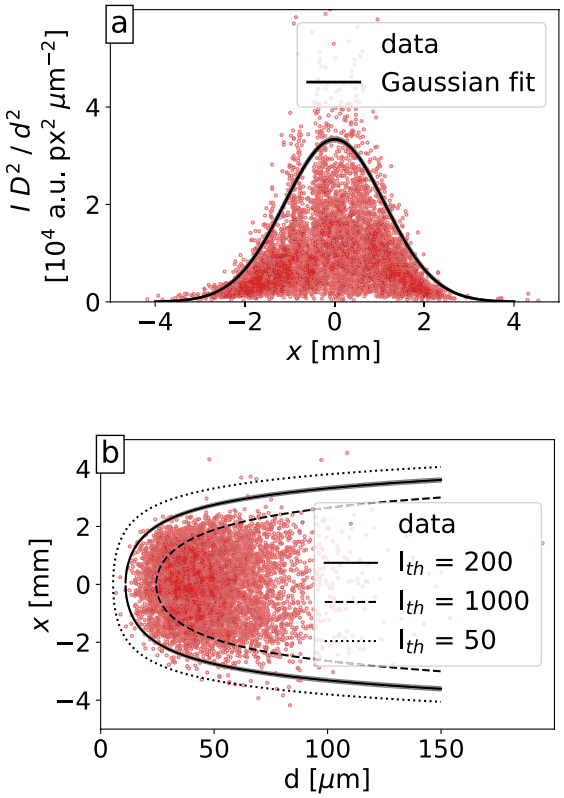

Fig. 12 (**a**) Scatter plot of the normalized intensity of the microbubbles versus their distance from the center of the laser beam in x-direction; (**b**) the expected edge size δ_{edge} of the measurement volume in the x-direction, as a function of the microbubble diameter. The measured microbubble positions are included for comparison

Eq. 5, the maximum values in the graph in Fig. 12a follow a Gaussian profile. We divide the x-direction into 200 bins and determine the 95th percentile of ID^2/d^2 for each bin to estimate the normalized intensity maximum, after which we fit a Gaussian profile through these maximum values. From this procedure, we find $\tilde{I}_0 = 33383 \pm 501$ a.u. px^2 μm^{-2} and $\delta_b = 1.577 \pm 0.027$ mm. The uncertainties on these parameters are the variances in the parameters according to the regression algorithm used for the fitting procedure[5].

Figure 12b shows the influence of the intensity threshold I_{th} on the edge size δ_{edge}. An increase in I_{th} results in a decrease in the measurement volume, and it increases the diameter of the smallest detectable microbubble. This results in a shift of the measurement range of the IPI setup toward larger microbubble diameters.

Using the parameters $\tilde{I}_0$ and δ_b, we can estimate the measurement volume for IPI. To show the influence of the

[5] We use *curve_fit* from the *SciPy* library (Virtanen et al. 2020) to fit the curve.

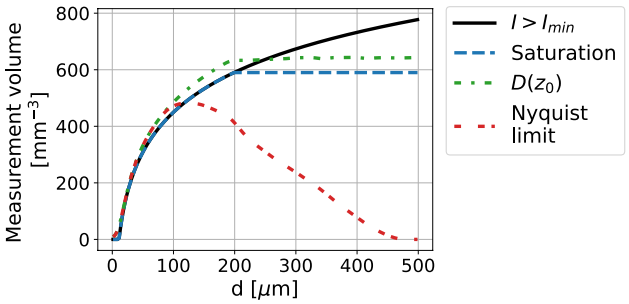

Fig. 13 The IPI measurement volume for four different cases, with increasing complexity: The measurement volume only from the intensity threshold; including saturation effect; including variation in D; including the Nyquist limit

variation in D, the saturation and the Nyquist limit, we determine the measurement volume in all these cases, as shown in Fig. 13. The black solid line shows the measurement volume when only the intensity threshold is taken into account. The blue dashed line adds the saturation effect, resulting in a constant measurement volume for $d > d_S$. The green dashed line adds the effect of variations in D, increasing the measurement volume slightly. And finally, adding the effect of the Nyquist limit results in the red dashed line.

The influence of the Nyquist limit is already significant at relatively small microbubble diameters ($d \approx 100$ µm) and causes the measurement volume to drop to zero at a certain maximum diameter d_{max}. Using the method explained in Sect. 3.1, we can determine d_{max} as 475 µm. According to Eq. 9, the minimum detectable diameter is $d_{min} = 7.9$ µm, while Eq. 10 sets the lower limit at $d_{min,I} = 13.7$ µm for $I_{th} = 300$. Equation 8 shows that saturation can happen for microbubble diameters larger than $d_S = 202.3$ µm.

Errors in the detection of microbubbles contribute to the uncertainty in the concentration, which is not easy to quantify. An attempt is made by Nobach et al. (2002), who give a derivation of the probability that two microbubble images overlap. Overlap can lead to erroneous results for the localization of the microbubble images, or even could cause the microbubble images to be overlooked by the processing algorithm. This leads to an underestimation of the microbubble concentration. Previous authors tried to reduce the overlap using an optical compression technique, reducing the circular microbubble image to a thin rectangular image (Maeda et al. 2000; Kawaguchi et al. 2002). However, knowledge of the full microbubble image is necessary to determine the fringe orientation.

We choose to reduce the negative implications of overlap by removing the overlapping parts of the microbubbles before calculating the fringe pattern (Damaschke et al. 2005). Furthermore, to quantify the detection errors we manually identify 3453 objects in 150 images, and determine their position and approximate radius, as well

as whether their fringe pattern corresponds to a bubble. From these 3453 objects, we find 3199 objects that exhibit a clear fringe pattern. The 254 objects that do not present a correct fringe pattern are classified as speckle patterns (184), tilted fringe patterns (41), and holograms (29).

From the 3269 objects with a clear fringe pattern, a tilted fringe pattern or a hologram, 1017 objects have a higher intensity than $I_{th} = 300$ counts. So, by eye (manually) we detect 1017 microbubbles in 150 images. However, our algorithm only detects 799 microbubbles when applying the same restrictions. We therefore multiply the IPI concentration by a correction factor of $1017/799 = 1.273$.

This error due to the algorithm performance can be broken down into two parts, i.e., one associated with microbubble image detection and one with the post-processing of the fringe pattern. The algorithm detected 905 microbubble images having $I_{th} > 300$ counts, which means that the image detection part was responsible for 112 of the 218 missing microbubbles. The other 106 missing microbubbles could be explained by the algorithm not being able to resolve the fringe spacing correctly. Increasing I_{th} reduces both types of errors, but especially the image detection error. The disadvantage of increasing I_{th} is that it reduces the measurement volume (Fig. 12b) and increases the minimum detectable microbubble diameter, as shown in Eq. 10.

Decreasing the amount of overlap would also reduce both types of errors. From the manually detected microbubbles, we find that 1535 objects appear to overlap with other objects, which is close to 44% of the total number of detected objects. This is a relatively high fraction and might indicate that the microbubble concentration during the experiment was close to the upper limit of what IPI is capable of dealing with.

The 2-D FFT method shows its strength in distinguishing solid particles from microbubbles. From the 184 speckle patterns, 179 are discarded for not respecting the condition on the fringe orientation.

Besides the detection error, we also analyze the propagation of the uncertainty on the individual parameters into the total uncertainty on the concentration. To this purpose, we use a Monte–Carlo method. We compute 10000 times the microbubble concentration using estimates from the involved physical parameters, whose values are taken randomly within their own uncertainty ranges. This number of realizations of the concentration is deemed sufficient for both the average and standard deviation to converge, such that an additional realization would only change the average and standard deviation of the concentration by less than 0.1%.

From this analysis, we conclude that the uncertainty in λ and K is negligible. For a better insight, we divide the different uncertainty sources into three groups, i.e., the uncertainty source from parameters that define the particle diameter d (K, D, λ, z_1), the uncertainty source from parameters that define the measurement volume ($\tilde{I}_0$, δ_b), and the uncertainty source from statistics (the limited amount of microbubbles that could be detected). We determine the uncertainty propagation of these sources by evaluating the measured concentration while setting the uncertainties of the other groups zero.

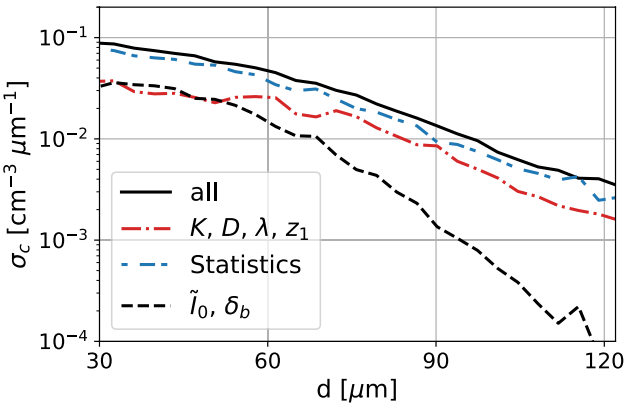

Fig. 14 Different uncertainty contributions to the total uncertainty in the microbubble concentration, σ_c, i.e., uncertainty in parameters corresponding to the microbubble diameter estimation (K, D, λ, z_1); uncertainty due to statistics; uncertainty in parameters corresponding to the measurement volume estimation ($\tilde{I}_0$, δ_b)

Figure 14 shows the resulting uncertainties in the concentration defined as the standard deviation over the 10000 concentration realizations. From this graph, it is clear that the uncertainty due to limited statistics is dominant. Increasing the number of detected microbubbles will also reduce the error in the measurement volume, because the fitting procedure of $\tilde{I}_0$ and δ_b might become more accurate.

From the analysis, we also find that the diameter range of the concentration spectrum plays an important role in the final uncertainty. A smaller diameter bin width results in less counts and therefore a larger error in the estimate of the number of microbubbles. Additionally, with a smaller bin size the probability that a microbubble can also be distributed into a different diameter bin due to the uncertainty in d increases.

4.2 Calibration of LMS

The normalized contrast C_M^0 is necessary to compute both the microbubble diameter (using Eq. 15) and the measurement volume (using Eq. 18). In order to compute C_M^0, we determine τ using a bootstrapping method, which resulted in $\tau = 0.082 \pm 0.005$.

As explained in Sect. 3.3, small microbubble images are increasingly harder to detect when χ grows, which results in a loss of detected microbubbles for relatively high values of

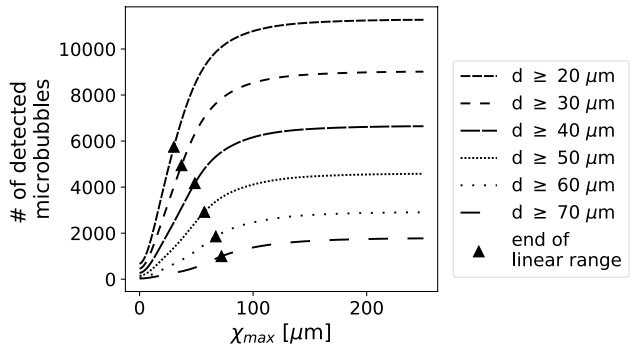

Fig. 15 The number of microbubbles found within a depth defined by χ_{max}. The diameters in the legend represent the minimum diameter of the microbubbles to be included

χ. Figure 15 shows the relationship between χ and the number of microbubbles found, for different ranges of microbubble diameters. Assuming a spatially constant microbubble concentration and a linear relationship between χ and z_0, we expect a linear relationship between χ and the detected number of microbubbles as well. The triangles in Fig. 15 represent the points where the curve appears to flatten due to loss of detection. These triangles are therefore possible definitions of χ_{max}. This definition of χ_{max} depends on the minimum microbubble diameter of interest. We are interested in microbubbles with a diameter larger than 30 µm, which results in $\chi_{max} = 38.22$ µm.

The relationship between χ and z_0 is calibrated by moving a calibration plate with black dots over a range of positions in z-direction. Figure 16a shows that the relationship between χ and z_0 is linear for $|z_0| < 4$ mm. From this figure, we obtain that $\chi_{max} = 38.22$ µm corresponds to $\Delta z_0 = 4.02 \pm 0.14$ mm. To check whether this calibration procedure is also applicable for microbubbles, we obtain the z_0-coordinate of the LMS microbubbles from the IPI images. Figure 16a shows the median value of the microbubbles' χ value corresponding to that z_0 coordinate. There is strong agreement between $\chi(z_0)$ for calibration dots and microbubbles if $\chi < 40$ µm.

The magnification is calculated from the calibration plate located at $z_0 = 0$. Because it is unclear at what side of the focal plane a defocused microbubble is located, we take into account the variation of the magnification over Δz_0. From this analysis, we find a pixel size in the object plane of 2.390 ± 0.019 µm. We neglect the microbubbles at 100 px from the edge, reducing the field of view (FoV) to 1960 times 2360 px. Multiplying the area of this FoV in the object plane with Δz_0 results in a measurement volume of $106.2 \pm 4.0\,\text{mm}^3$, where the variance in the measurement volume is found from combining the variances in each dimension.

To validate the theoretical description for $p_l(C_M^0)$, we make a comparison with the trends obtained using

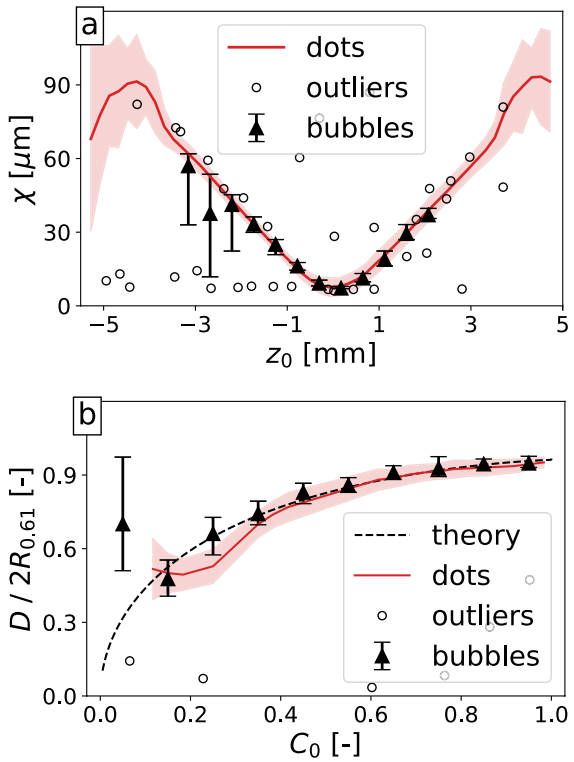

Fig. 16 (**a**) The blur radius χ as function of out-of-focus depth, for microbubbles and calibration dots. (**b**) The ratio between $d/2R_l$ as a function of the normalized contrast C_M^0. The shaded area represents one standard deviation for the calibration case, the black caps represents one standard deviation for the case of the microbubbles. The outliers are microbubbles that fall outside the 1^{st} or 99^{th} percentile

calibration dots and microbubbles, similar as we did for the $\chi(z_0)$ case above. We determine the size of the LMS microbubble image from the IPI counterpart. Figure 16b shows the comparison of $D/2R_l$ versus C_M^0 for both calibration dots and microbubbles, and the black line representing the theoretical relationship from Fdida and Blaisot (2010). The experimental data agree with the theoretical prediction for $C_M^0 > 0.3$.

The uncertainty in $p_l(C_M^0)$ is determined from the variance in the estimation according to the calibration dots, as is visualized by the shaded area in Fig. 16b. After removing the outliers, we can approximate the uncertainty by a linear relation $\sigma_{p_l} = -0.0205 C_M^0 + 0.0289$ for $C_M^0 > 0.3$. For $C_M^0 < 0.3$, the uncertainty grows exponentially and the estimate of D becomes unreliable. Equation 15 shows that the uncertainties in the magnification and in $p_l(C_M^0)$ will propagate into the uncertainty in the diameter. From the uncertainties found above, we can compute a maximum relative uncertainty of 3.4% in the estimated diameter at $C_0 = 0.3$.

The microbubble image is discretized, resulting in an uncertainty in the estimation of the microbubble image area A. The estimation of this uncertainty is known as the

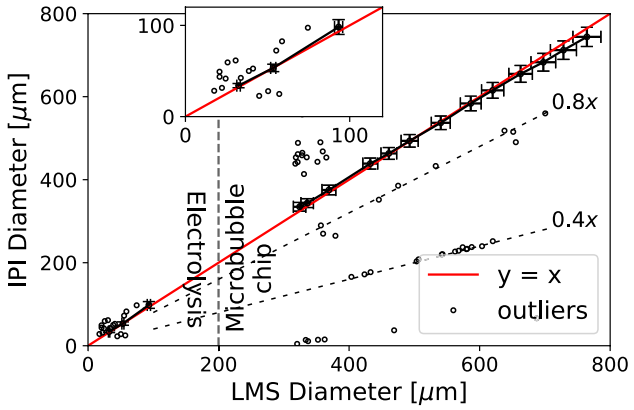

Fig. 17 Comparison between the microbubble diameters measured by long-range microscopic shadowgraphy and interferometric particle imaging. The open circles represent outliers. A number of these outliers seem to follow a linear trend, i.e., $d_{IPI} = 0.8\ d_{LMS}$ and $d_{IPI} = 0.4\ d_{LMS}$

Gaussian circle problem. Young (1988) shows that the error of the area estimate can be approximated by

$$\frac{|\text{Estimated Area} - \text{True Area}|}{\text{True Area}} = 0.585 D^{-1.6} \tag{22}$$

The uncertainty in the concentration from LMS is estimated in a similar way as for IPI. After 10000 different realizations of the concentration, both the mean concentration and its standard deviation are well converged.

5 Results

5.1 Microbubble sizes

The main results of this study concern the validation of microbubble sizes and concentrations as obtained from IPI using the estimates from LMS. Figure 17 shows the estimated microbubble size from IPI compared with the estimation from LMS. The inset focuses on the results for the electrolysis experiment, which generates microbubbles having a diameter $d < 100$ μm.

The shape of the microbubbles is guaranteed to be spherical even at the largest diameters (1000 μm) and velocities (10 cm s^{-1}). In this case, the Eötvös number ($Eo = \Delta\rho g d^2 \gamma^{-1}$) is equal to 0.14, where we assumed $\Delta\rho = 1000$ kg m^{-3}, $g = 9.81$ m s^{-2}, and the water surface tension $\gamma = 0.07$ N m^{-1}. The Reynolds number for this diameter and velocity is approximately $Re = Ud/\nu = 100$, where we assumed $\nu = 10^{-6}$ m^2 s^{-1}. For these Eötvös and Reynolds numbers, the microbubble is still in the spherical regime (Clift et al. 1978).

In the analysis, we only accepted microbubble images for which the orientation deviates at most 2.86° from the expected orientation, the SNR$N_s \geq 15$ dB, $I_{th} \geq 100$ counts, and where the overlap does not hamper the application of the identification algorithm. We accept their LMS counterparts only when $C_M^0 \geq 0.3$ and $\epsilon > 0.9$. As a first observation, estimates of the microbubble diameters from both IPI and LMS agree well, except at the largest diameters under investigation ($d \geq 700$ μm), where IPI yields slightly smaller diameters as compared to LMS, though the difference remains within the level of uncertainty.

There is a low number of outliers (3.0% of the microbubbles), for which the diameters do not compare favorably. A part of these outliers follows a linear trend described by the line $d_{IPI} = 0.8\ d_{LMS}$ or its sub-harmonic $d_{IPI} = 0.4\ d_{LMS}$. It is unclear whether this is due to the fringe pattern itself not being perfectly sinusoidal, or due to the post-processing method. Without these outliers, the average of the difference between the IPI size estimation and the LMS size estimation for all microbubbles N_b is

$$\frac{1}{N_b}\sum_{i}^{N_b}\left|\frac{d_{IPI,i} - d_{LMS,i}}{d_{LMS,i}}\right| = 2.1\%. \tag{23}$$

5.2 Microbubble concentration

Figure 18 shows the microbubble concentration as a function of the diameter, for both IPI and LMS. Similar detection limits are applied as for the diameter comparison case. Microbubble images are retained when the fringe orientation is at most 2.86° off, SNR$N_s \geq 15$ dB, and $I_{th} \geq 300$ counts. LMS microbubbles are accepted when $C_M^0 \geq 0.3$, $\chi \leq \chi_{max}$, $d \geq 30$ μm, and $\epsilon > 0.9$. For both cases, microbubbles within 100 px from the edge are not included. Due to these restrictions, 6365 IPI microbubbles and 3671 LMS microbubbles are accepted out of, respectively, 9312 and 14865 objects which were detected in 1000 images. The IPI concentration is multiplied by a correction factor of 1.273 to account for erroneous detection and post-processing (see Sect. 4.1).

The influence of the Nyquist limit on the measurement volume became significant for microbubbles with a diameter larger than 100 μm, as is shown in Fig. 13. The maximum microbubble diameter measured is approximately 120 μm, but the concentration at diameters above 90 μm is two orders of magnitude smaller compared with the concentration in the range $30 \leq d \leq 50$ μm. This implies that the concentration overestimation from the aliasing effect is negligible.

The concentration spectra found by LMS and IPI are very similar and fall within each others uncertainty range, as defined by the 5^{th} to 95^{th} percentile. Figure 18a shows the concentrations in linear scale, which shows that both

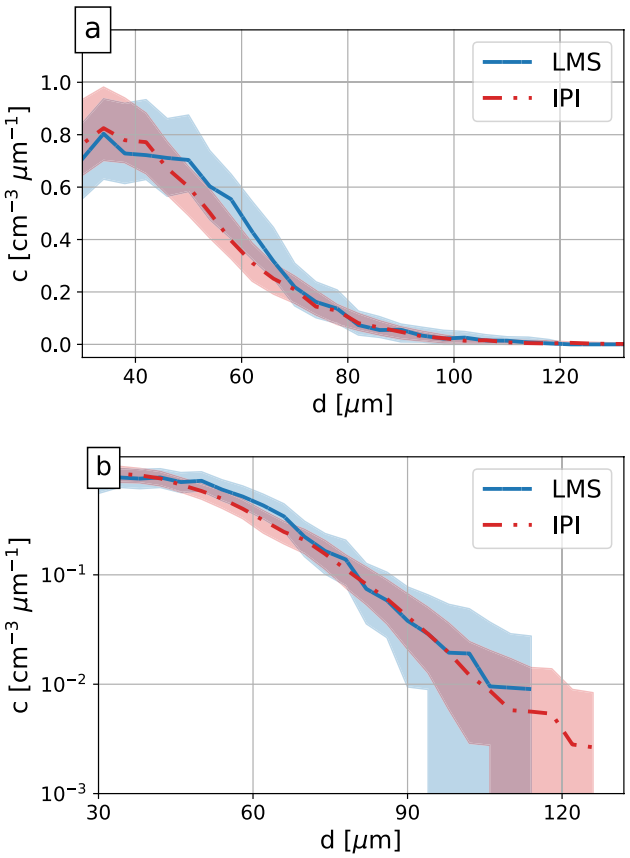

Fig. 18 Comparison between the microbubble concentrations measured by long-range microscopic shadowgraphy and interferometric particle imaging. The shaded area describes the 5^{th} to 95^{th} percentile. (**a**) The concentrations in linear scale and (**b**) the concentrations in log-linear scale

measurement techniques present a very similar concentration spectrum shape. Because the concentration in the tail of the spectra is low, we also add the concentration spectrum in log-linear scale (Fig. 18b). In this representation, it is clear that the mean concentrations are very close to each other, even beyond 100 µm, although the number of detected bubbles is too low to estimate a nonzero value for the 5^{th} percentile of the concentration estimation.

6 Conclusion

In this study, the size and concentration of microbubbles are measured using two different techniques, i.e., interferometric particle imaging (IPI) and long-range microscopic shadowgraphy (LMS). The aim of this study is to validate the concentration as estimated from IPI and assess the uncertainty in such estimation.

We use LMS as an independent method to validate the IPI results. The IPI and LMS setups are designed such that the measurement volumes of both techniques overlap. Optical filters enable the simultaneous identification of the microbubbles with both methods. This way, identical microbubbles could be detected and identified in images captured with both techniques. The experimental methodology enabled therefore to validate the microbubble size estimation with respect to the result from LMS. The difference between the estimated size from IPI and LMS over a diameter range of 10 - 800 µm was only of 2.1%.

We show that the diameter range of the IPI technique is limited among other parameters by the dynamic range of the camera (Eq. 10) and that this limit can be more stringent than the limit often shown in the literature (Eq. 9), which is based on the maximum detectable fringe spacing.

Additionally, we show that, for IPI microbubbles, the variation of the image size D in the defocus direction z_0 should not be neglected. Due to this variation, the diameter range, as limited by the Nyquist criterion, depends on the position of the microbubble in the measurement volume. This causes the measurement volume to decrease significantly already at smaller microbubble diameters than expected when assuming D to be constant.

We find similar uncertainty levels in the estimated concentration of both IPI and LMS, of the order of 5 - 10% of the estimated concentration. The statistical error is the largest contributor to this uncertainty, due to the small amount of microbubbles detected (6365 microbubbles according to IPI and 3671 microbubbles according to LMS). The error in the detection algorithm of IPI was quantified, resulting in a correction factor of 1.273 for the IPI concentration.

Finally, we find that the estimated concentration from IPI agrees with the estimated concentration from LMS within the uncertainty range. The agreement held over the complete range of measured microbubble diameters considered in the experiment, and for which the techniques were calibrated. From this, we can therefore argue that IPI is able to reliably estimate the microbubble concentration.

Acknowledgements We are thankful to Milos Birvalski and Martijn van Rijsbergen from MARIN, Wageningen, for the valuable discussions that led to improve the quality of this work. We are also grateful to them for lending their microfluidic equipment. The contribution of Gert Dekkers during the experimental campaign is also acknowledged.

Author Contributions R. Stigter did conceptualization, methodology, formal analysis and investigation, and software. R. Stigter and D. Fiscaletti did writing—original draft; D. Fiscaletti and G. Elsinga performed supervision and writing – review & editing; T. van Terwisga and J. Westerweel contributed to funding acquisition and writing—review & editing and supervision.

Funding This publication is part of the project AQUA (with project number P17-07) of the research programme Perspectief which is (partly) financed by the Dutch Research Council (NWO).

Data availability The experimental data obtained for this study are accessible upon reasonable request, by contacting the corresponding author.

Declarations

Conflict of interest The authors declare no conflict of interest.

References

Adrian RJ, Durão DFG, Durst F, et al. (1991) Applications of Laser Techniques to Fluid Mechanics. In: Applications of Laser Techniques to Fluid Mechanics. Springer Berlin Heidelberg, https://doi.org/10.1007/978-3-642-61254-1

Birvalski M, van Rijsbergen MX (2017) Exploratory measurements of cavitation nuclei in the wake of a ship. 5th International Conference on Advanced Model Measurement Technology for the Maritime Industry (AMT17), Glasgow, Scotland

Birvalski M, van Rijsbergen MX (2018) Application of Interferometric Particle Imaging to cavitation nuclei measurements in a ship model basin. 19th International Symposium on the Application of Laser and Imaging Techniques to Fluid Mechanics, Lisbon, Portugal

Birvalski M, Boucheron R, van Rijsbergen M, et al. (2019) Developments in micro-bubble measurement techniques for cavitation and PIV experiments. 6th International Conference on Advanced Model Measurement Technology for the Maritime Industry, Rome, Italy

Blaisot JB, Yon J (2005) Droplet size and morphology characterization for dense sprays by image processing: application to the Diesel spray. Exp Fluids 39(6):977–994. https://doi.org/10.1007/s00348-005-0026-4

Bradski G (2000) The OpenCV Library. Dr Dobb's Journal of Software Tools

Brandner PA (2018) Microbubbles and Cavitation: Microscales to Macroscales. In: Proceedings of the 10th international symposium on cavitation (CAV2018). ASME press

Brandner PA, Venning JA, Pearce BW (2022) Nucleation effects on cavitation about a sphere. J Fluid Mech 946:A1

Clift R, Grace J, Weber M (1978) Bubbles. Dover Publications Inc, Mineola, New York, Drops and Particles

Damaschke N, Nobach H, Nonn TI et al (2005) Multi-dimensional particle sizing techniques. Exp Fluids 39(2):336–350. https://doi.org/10.1007/s00348-005-1009-1

Dehaeck S, Van Beeck JPAJ (2007) Designing a maximum precision interferometric particle imaging set-up. Exp Fluids 42(5):767–781. https://doi.org/10.1007/s00348-007-0286-2

Duda RO, Hart PE (1972) Use of the hough transformation to detect lines and curves in pictures. Commun ACM 15(1):11–15. https://doi.org/10.1145/361237.361242

Ebert E, Kröger W, Damaschke N (2015) Hydrodynamic Nuclei Concentration Technique in Cavitation Research and Comparison to Phase-Doppler Measurements. J Phys: Conf Ser 656:012111. https://doi.org/10.1088/1742-6596/656/1/012111

Fdida N, Blaisot JB (2010) Drop size distribution measured by imaging: Determination of the measurement volume by the calibration of the point spread function. Meas Sci Technol 21(2):025501. https://doi.org/10.1088/0957-0233/21/2/025501

Friesch J, Kim KH, Andersen P, et al. (2002) The specialist committee on water quality and cavitation, final report and recommendations to the 23rd ittc. 23rd International Towing Tank Conference II:451–483

Graßmann A, Peters F (2004) Size measurement of very small spherical particles by Mie scattering imaging (MSI). Part Part Syst Charact 21(5):379–389. https://doi.org/10.1002/ppsc.200400894

Ibrahim KM, Wertheimer GD, Bachalo WD (1991) Signal Processing Considerations for Low Signal to Noise Ratio Laser Doppler and Phase Doppler Signals. In: Laser Anemometry - Advances and Applications 1991; Proceedings of the 4th International Conference

Kawaguchi T, Akasaka Y, Maeda M (2002) Size measurements of droplets and bubbles by advanced interferometric laser imaging technique. Meas Sci Technol 13(3):308–316. https://doi.org/10.1088/0957-0233/13/3/312

Khoo MT, Venning JA, Pearce BW et al (2020) Natural nuclei population dynamics in cavitation tunnels. Exp Fluids 61(2):34. https://doi.org/10.1007/s00348-019-2843-x

König G, Anders K, Frohn A (1986) A new light-scattering technique to measure the diameter of periodically generated moving droplets. J Aerosol Sci 17(2):157–167. https://doi.org/10.1016/0021-8502(86)90063-7

Lebrun D, Ozkul C, Touil CE, et al. (1993) On-line particle size and velocity measurements by the analysis of defocused images: Extended depth of field. In: Downs MJ (ed) Proceedings of SPIE 2088, Laser Dimensional Metrology, Brighton, United Kingdom, pp 139–148, https://doi.org/10.1117/12.168074

Maeda M, Kawaguchi T, Hishida K (2000) Novel interferometric measurement of size and velocity distributions of spherical particles in fluid flows. Meas Sci Technol 11(12):L13–L18. https://doi.org/10.1088/0957-0233/11/12/101

Medwin H (1977) Counting bubbles acoustically: a review. Ultrasonics 15(1):7–13. https://doi.org/10.1016/0041-624X(77)90005-1

Mees L, Lebrun D, Allano D, et al (2010) Development of interferometric techniques for nuclei size measurement in cavitation tunnel. Pasadena, California, United States, Hal-02414550

Nobach H, Damaschke N, Tropea C (2002) Optical limits of particle concentration for multi-dimensional particle sizing techniques in fluid mechanics. Exp Fluids 32(2):143–152. https://doi.org/10.1007/s00348-001-0371-x

Oldenziel DM (1982) A new instrument in cavitation research: the cavitation susceptibility meter. J Fluids Eng 104(2):136–141. https://doi.org/10.1115/1.3241790

Pentland AP (1987) A New Sense for Depth of Field. IEEE Trans Pattern Anal Mach Intell PAMI-9(4):523–531. https://doi.org/10.1109/TPAMI.1987.4767940

Russell P, Venning J, Pearce BW et al (2020) Calibration of Mie scattering imaging for microbubble measurement in hydrodynamic test facilities. Exp Fluids 61(4):93. https://doi.org/10.1007/s00348-020-2927-7

Shinpaugh KA, Simpson RL, Wicks AL et al (1992) Signal-processing techniques for low signal-to-noise ratio laser Doppler velocimetry signals. Exp Fluids 12–12(4–5):319–328. https://doi.org/10.1007/BF00187310

Stigter R, Birvalski M, Schouten R, et al. (2024) An early assessment of the effect of water quality and sea-state on propeller cavitation inception of a full-scale vessel. 12th International Cavitation Symposium - CAV2024, Chania, Greece

Sumlin BJ, Heinson WR, Chakrabarty RK (2018) Retrieving the aerosol complex refractive index using pymiescatt: a mie computational package with visualization capabilities. J Quant Spectrosc Radiat Transfer 205:127–134.

Thorpe S (1982) On the clouds of bubbles formed by breaking windwaves in deep water, and their role in air - sea gas transfer. Philos Trans R Soc London Ser A Math Phys Sci 304(1483):155–210.

Virtanen P, Gommers R, Oliphant TE et al (2020) SciPy 1.0: fundamental algorithms for scientific computing in Python. Nat Methods 17:261–272. https://doi.org/10.1038/s41592-019-0686-2

Young IT (1988) Sampling density and quantitative microscopy. Anal Quant Cytol Histol 10(4):269–274

Zangwill A (2013) Modern electrodynamics. Cambridge University Press, Cambridge, UK